J. Fluid Mech. (2021), *vol*. 926, A19, doi:10.1017/jfm.2021.719

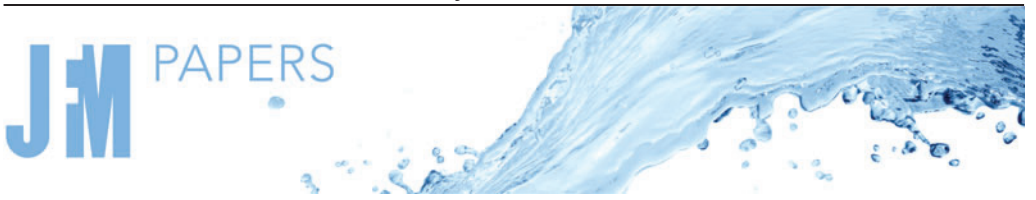

Soap film catastrophes

Hamed K. Habibi[1] **and Rouslan Krechetnikov**[1],†

[1]Mathematical and Statistical Sciences, University of Alberta, Edmonton, AB T6G 2G1, Canada

(Received 31 January 2021; revised 22 June 2021; accepted 10 August 2021)

Earlier systematic experimental studies of bursting soap films by McEntee & Mysels (*J. Phys. Chem.*, vol. 73, 1969, pp. 3018–3028) revealed the existence of a precursor shock wave preceding the expanding hole in a punctured film, with a disturbed region of shrinking film material in between known as the 'aureole'. In the present work we report and interpret new phenomena associated with the aureole – the formation of folds on the surface of soap films. In search of the theoretical explanation of the experimentally identified conditions under which the folds appear, we establish that they correspond to catastrophes of collapsing soap films.

Key words: thin films

1. Introduction

Soap bubbles made of thin surfactant-laden films have been not only the object of children's play, but also the subject of scientific research since the time of Leonardo da Vinci (Maxwell 1878; Burkhardt 2021). As presently known, soap films – a constituting element of soap bubbles and foams – represent complex phenomena with sophisticated physics governing their existence and dynamics. After Robert Hooke in 1672 brought to the attention of the Royal Society the optical phenomena they exhibit (Birch 1757), soap films stimulated the development of the theories of optics (Newton 1704), capillarity (Plateau 1873) including thin-film drainage (Gibbs 1928, 1931), and minimal surfaces (Plateau 1873; Douglas 1931; Courant & Robbins 1941; Almgren & Taylor 1976). At the same time, soap films served as a tool for detecting the magnetism of gases (Faraday 1851), as an analogue computer for solving boundary-value problems (Prandtl 1903; Johnston 1935), and in elucidating a number of problems in surface and colloid chemistry (Mysels 1964), such as phase transitions in monolayers and film elasticity. Owing to a high degree of two-dimensionality, soap or other freely suspended thin liquid films have also been used for studying hydrodynamics and turbulence (Couder, Chomaz & Rabaud 1989; Gharib & Derango 1989) in two dimensions as well as shock wave (SW) dynamics (Wen, Chang-Jian & Chuang 2003), since certain features of the soap film flow do resemble those anticipated

† Email address for correspondence: krechet@ualberta.ca

for a true planar flow. The never-ending interest in thought-provoking soap film phenomena is not only reflected in comprehensive review articles (Mysels, Shinoda & Frankel 1959; Rusanov & Krotov 1979), but also culminated in popularizing books (Boys 1890; Isenberg 1992).

In the context of prehistory to the present study, it should be mentioned that McEntee & Mysels (1969), who studied bursting soap films using high-speed flash photography, revealed the presence of a precursor SW preceding the expanding hole in a punctured film. The disturbed region of shrinking film material in between the SW and the hole is usually referred to as the 'aureole', which was shown (Frankel & Mysels 1969) to be related to large variations in surface tension as the film retracts and thickens. These important observations overturned some misconceptions regarding the bursting process in earlier theoretical and experimental works (Dupré 1867; Plateau 1873), which assumed that a rolled-up rim collects all of the disappearing film, leaving the rest of the film undisturbed (Taylor 1959*b*). In the present study, we report new phenomena associated with the aureole and offer theoretical insights into the underlying mechanisms.

The paper is organized as follows. In § 2 we discuss the experimental platform and the preparation of the soap solutions. Experimental observations of folds on soap films and detailed measurements of the kinematic conditions under which the phenomena occur are reported in § 3.1. The discussion of possible underlying mechanisms in § 3.2 accompanied by extra experiments testing the effect of the soap film frame geometry leads to a paradox, which is resolved theoretically in § 4 by modelling the soap film dynamics and analysing the corresponding governing equations. Further discussion of the underlying mechanisms in § 5 reveals that the appearance of folds can be interpreted under the umbrella of catastrophe theory.

2. Experimental apparatus and procedure

The main components of the experimental set-up shown schematically in figure 1 include the wire frame, its withdrawal mechanism for creating the soap film (not shown), film thickness measurement system, film release electrical circuit by Joule heating (Mayer & Krechetnikov 2017) and high-speed visualization.

To achieve a wide range of dynamic viscosities $\mu = 1.16$–2.13 mPa s, surface tensions $\sigma = 35$–47.6 mN m^{-1} and film thicknesses $h_\infty = 4.6$–19.3 μm, we prepared soap solutions using ultrapure water (Millipore Direct-Q 3UV-R) with various concentrations of glycerol ($C_g = 5$–25 % wt) and an anionic surfactant, sodium dodecyl sulphate (SDS; $C = 0.5$–1.25 of the critical micelle concentration, CMC) with purity ≥ 99.5 % (Sigma-Aldrich 75746) as well as five different wire frame withdrawal velocities V in the range 5–16.1 mm s^{-1}. SDS was chosen for several reasons, one being that it is well characterized and has been used in a number of fluid interface studies (Mysels & Cox 1962; Lyklema, Scholten & Mysels 1965; McEntee & Mysels 1969; Evers, Shulepov & Frens 1996; Huibers & Shah 1997; Berg, Adelizzi & Troian 2005). While the primary use of glycerol is to stabilize the soap film (Mayer & Krechetnikov 2017) and control its thickness, the addition of glycerol may also lead to extraneous ramifications, such as affecting the characteristic time τ of settling the edge retraction velocity U_{TC} (Savva & Bush 2009) and the kinetics of SDS (Khan *et al.* 2019). With regard to the former effect, for the glycerol concentrations used in our experiments, the associated Ohnesorge numbers are low, $Oh = \mu/\sqrt{2h_\infty \rho\sigma} < 0.1$, with ρ being the density of the liquid, so the time scale τ is dictated by the inviscid dynamics, $\tau_{inv} = \sqrt{\rho h_\infty^3/\sigma} = O(10)$ μs, since the viscous time scale is much shorter, $\tau_{visc} = \mu h_\infty/2\sigma = O(0.1)$ μs. As for the latter effect,

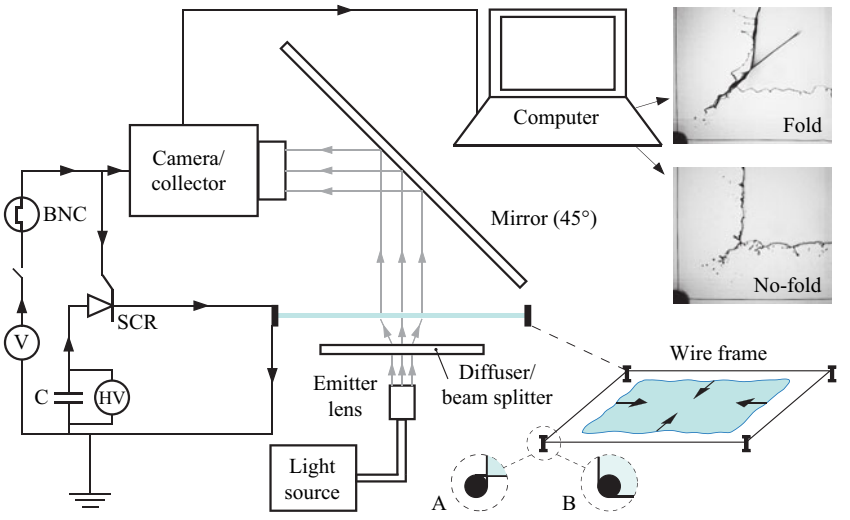

Figure 1. The experimental apparatus. Once a capacitor (C) is charged with a high-voltage power supply (HV), a low-voltage power supply (V) sends a 5 V trigger signal to a pulse/delay generator (BNC), which, after a precisely predefined delay, sends a triggering signal to the high-speed camera and thyristor (SCR). Then, the high-speed camera starts recording and the thyristor releases the energy stored in the capacitor to the wire frame and the soap film retracts due to instant boiling on the wire. Before the soap film retraction stage, the thickness of the soap film is measured using a spectrometer consisting of light source, emitter lens and collector.

the CMC of SDS increases with addition of glycerol, though this change is insignificant for the concentrations used in our experiments: CMC changes in the range 8.05–8.20 for $C_g = 0 - 20\,\%$ (cf. Carnero Ruiz, Diaz-Lopez & Aguiar 2008), though alternative measurements by Khan *et al.* (2019) suggest that the CMC decreases with glycerol added up to $C_g = 20\,\%$. The change of CMC in turn affects the adsorption isotherm; cf. figure 2(*a*) in Fernandez, Krechetnikov & Homsy (2005) or figure 5 in Tajima, Muramatsu & Sasaki (1970).

The soap film is formed on a continuous conducting wire (NiC 60, Pelican Wire Co.) with well-characterized properties (Incropera & DeWitt 2002), which is strung around four aluminium posts (DU-BRO brand E/Z connectors) forming the frame capable of adjusting different aspect ratios of a rectangular geometry $l_1 \times l_2$, though in most of the reported experiments a square frame was employed with side $l = 50$ mm. The wire ends are held in place using a clamp manually adjusted to have the wire frame aptly tensioned. Two different configurations of the wire mounted at the corners are used to study the effect of sharp (A) and round (B) corners on the outcome of the soap film patterns. The soap film withdrawal mechanism was contrived and built with the help of two precision stepper motor assemblies (linear Velmex BiSlide and rotary Velmex B5990TS), which are controlled and programmed by Velmex COSMOS software, in order to perform two major tasks: (i) to raise and lower the bath with a soap film solution while keeping the frame stationary (tantamount to dipping the frame assembly in a bath with soap solution and withdrawing it at a known predefined speed); and (ii) to rotate the fresh soap film formed on the wire frame to a horizontal position. The horizontal orientation of the soap film was preferred to minimize gradual thinning due to gravity, which was already known and described by Newton (1704).

Once the soap film is positioned horizontally, after $\sim$1 s two steps take place in parallel (the delay is to let the soap film stabilize in the horizontal orientation and relax

possible motions in the film caused during the rotation step). First, the soap film is released by impulsive Joule heating of the frame wire (Mayer & Krechetnikov 2017). The energy required for the impulsive heating is stored in a capacitor (C) and delivered to the wire through a thyristor (SCR) in a single high-voltage 2.4 kV electrical pulse. A schematic diagram of the electrical circuit used in the experimental set-up is shown in figure 1. The conducting soap film frame forms two parallel resistors of total resistance 1.2×10^{-6} Ω m. Two high-voltage capacitors (Condenser Products MQP105-5MN, 1 mF, 5 kV), which are connected in series to form C, are charged with a high-voltage power supply (HV; Matsusada, EQ-30P1-LG) to the desired value $\varphi = 2.4$ kV. Upon charging, a low-voltage power supply (V; Instek GPD-3303S) sends a 5 V electrical signal to a pulse/delay generator (BNC; Berkeley Nucleonics Corp., Model 575). Second, after some delay precisely set by the BNC, a 5 V trigger pulse is sent to the high-speed camera (Vision Research, Phantom V5.2) and the thyristor SCR (Astrol Electronics AG, AC-10140-001). The camera starts recording upon receiving the trigger pulse and the thyristor closes the circuit, thus delivering the energy stored in the capacitor C to the wire frame. For visualization with high-speed photography, a back-lighting technique has been used: after the light emitted from the light source (a light-emitting diode (LED) lamp, LEDTronics PAR 38-12x2W-XPW-001S) passes through the optical diffuser plate and the soap film area of interest, it is reflected by the mirror positioned at 45° into the high-speed camera. Since the time of the soap film retraction is $<$10 ms, it was recorded at different frame rates (3000–5000 f.p.s.), exposure times ($\sim$30–100 μs) and resolutions by the high-speed camera with 35 mm and 55 mm Nikkor lens. For the particle image velocimetry (PIV) experiments, a dual-pulse Nd:YAG laser (Evergreen 200 mJ) served as a light source along with a 20X Arcturus^{TM} HeNe beam expander.

For evaluation of the steady retraction speed $U_{TC} = \sqrt{2\sigma/\rho h_\infty}$ of a soap film (Culick 1960; Taylor 1959*a*), one needs to know its thickness h_∞. However, despite being previously tested over a wide range of bulk and surface viscosities (Mysels & Cox 1962), Frankel's law (Mysels *et al.* 1959), i.e. $h_\infty = 1.88\sqrt{\sigma/\rho g}(\mu V/\sigma)^{2/3}$ for the thickness of a uniform film created in gravitational field g by vertical withdrawal of a wire frame with velocity V from a bath with surfactant solution having bulk viscosity μ and surface tension σ, demonstrates significant deviations. The deviations can be caused by drainage when the soap frame is in a vertical position in the stage of withdrawal or when the surfactant film is not expected (Adelizzi & Troian 2004) to be inextensible (though flexible) at $Ca \equiv \mu V/\sigma \gtrsim 10^{-3}$, thus violating the central assumption in the Frankel's law derivation.

The range of the capillary numbers Ca in our experiments is $O(10^{-4}$–$10^{-3})$. Therefore, an independent film thickness measurement was performed for all test conditions, in particular in order to evaluate theoretically the terminal velocity of the soap film retraction and various wave propagation velocities for comparison with the corresponding experimental values. Measurements of the soap film thickness were performed with the help of a collimated broadband light source (Dolan Jenner MI-150) as a light emitter, and a collimating lens/fibre optic cable (Thorlabs M25L02) as a collector of the light transmitted through the soap film, which in turn sends an optical signal to an ultraviolet–visible (UV-VIS) spectrometer (Ocean Optics USB4000-UV-VIS). A detailed explanation of the soap film thickness measurement can be found in Mayer & Krechetnikov (2017). For each test condition, the measurement was repeated three times and the average value reported, with the maximum deviation being $\sim$1 μm in all cases.

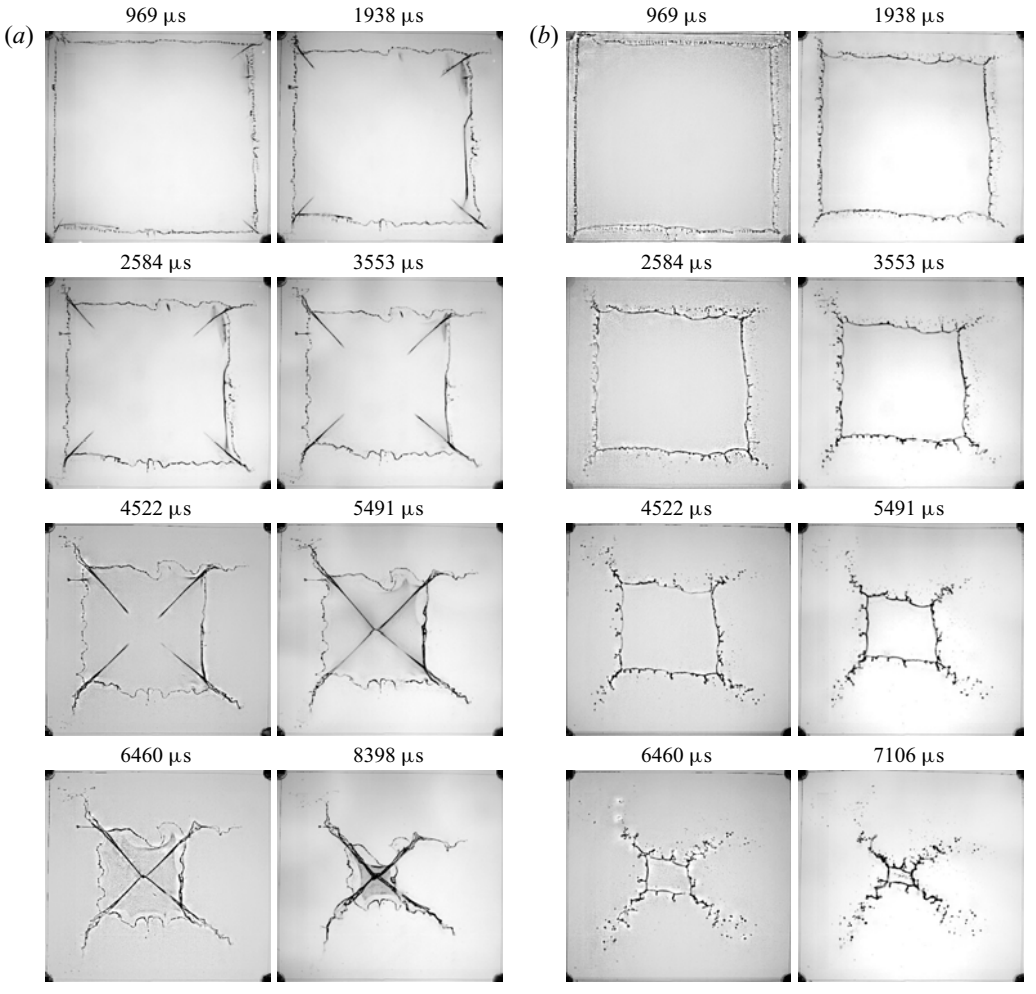

Figure 2. Fold (*a*) versus no-fold (*b*) patterns. (*a*) Time sequence of the soap film retraction with developing folds along the diagonal of the soap film surface. Soap film solution properties: 0.5 CMC of SDS, 20 % wt glycerol; soap film thickness and withdrawal velocity are 16.9 μm and 12.4 mm s^{-1}, respectively. (*b*) Time sequence of the soap film retraction without folds. Soap film solution properties: 1.25 CMC of SDS, 20 % wt glycerol; soap film thickness and withdrawal velocity are 8.5 μm and 12.4 mm s^{-1}, respectively. The physical image size in both sets of panels is 50 mm × 50 mm.

3. Experiments

3.1. *Observations*

In the course of repeating our earlier experiments to free up soap films from a rectangular wire frame (Mayer & Krechetnikov 2010*a*,*b*, 2017), we encountered the phenomena shown in figure 2, where two outcome patterns can be distinguished: (*a*) fold and (*b*) no-fold. While the fold may appear as a standing SW, it proves to be not so. In the fold pattern, SW-like lines along the soap film diagonal are formed shortly (∼1 ms) after the soap film is released from the wire frame. The folds propagate along the diagonal until they merge at the centre of the film (cf. figure 2*a*). In the no-fold pattern, the soap film simply retracts with the microdroplets dispatched from the soap film boundaries. Notably, the soap film

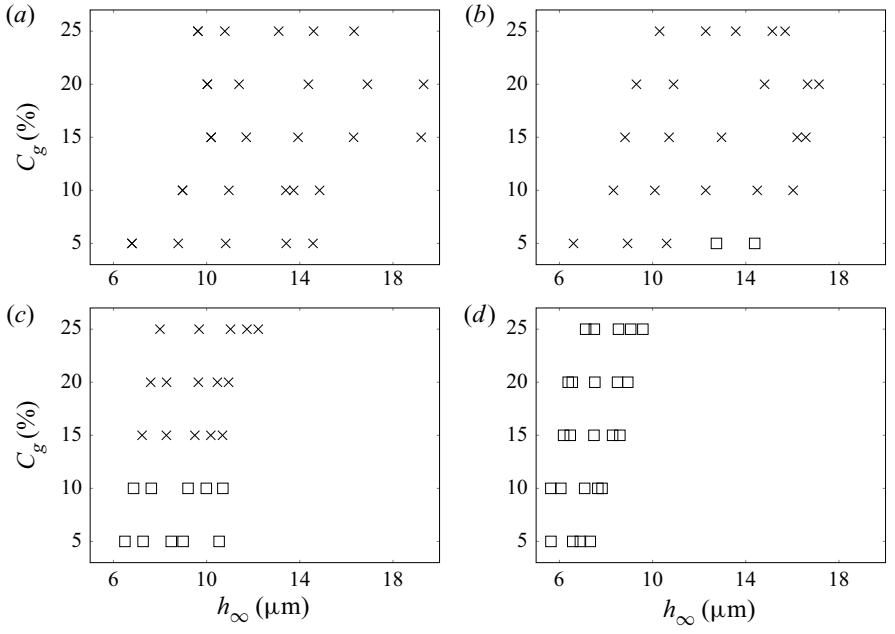

Figure 3. Maps of fold (×) and no-fold (□) patterns with respect to the soap film thickness for five different concentrations of glycerol, $C_g = 5,\ 10,\ 15,\ 20,\ 25\,\%\,wt$ and four concentrations of surfactant: (*a*) 0.5, (*b*) 0.75, (*c*) 1 and (*d*) 1.25 CMC.

retracts faster in the case of the no-fold pattern, which is especially evident at 6460 μ*s* by juxtaposing surface area of the soap films – the distinction being due to different values of soap film thickness.

It is known that the dynamics of the collapsing soap film is dictated by the soap solution properties (viscosity, surface tension, etc.) and the film thickness (Mysels *et al.* 1959; Couder *et al.* 1989; Brenner & Gueyffier 1999; Savva & Bush 2009). Therefore, a number of experiments were carried out to understand the transition between the fold and no-fold regimes depending upon the values of these parameters in a wide range, though limited by the soap film lifetime necessary to conduct the experiments. For that, the soap solution properties and withdrawal speed were varied as described in § 2. The corresponding maps of the transition in terms of glycerol concentration C_g with respect to the soap film thickness h_∞ are shown in figure 3. The variation in the soap film thickness along the horizontal axis is due to the change in the bath lowering speed. As evident from this figure by increasing SDS concentration the thickness of the soap film decreases, and the resultant pattern transitions from a fold to a no-fold.

To properly understand the physics underlying the fold to no-fold transition, the data in figure 3 are replotted in figure 4 in the key velocity coordinates. This figure demonstrates the relation between theoretically estimated one-dimensional wave propagation speed $c_0 = \sqrt{2E/\rho h_\infty}$, arising due to film Marangoni elasticity (Couder *et al.* 1989), and one-dimensional soap film retraction speed $U_{TC} = \sqrt{2\sigma/\rho h_\infty}$, calculated based on experimental values of the soap film surface tension σ, thickness h_∞ and elasticity $E = -2\,\mathrm{d}\sigma/\mathrm{d}\ln\Gamma$, where Γ is surfactant surface concentration. Data for surface tension $\sigma(\Gamma)$ were extracted from the study of Tajima *et al.* (1970). The use of the formula for elasticity in the Marangoni regime, i.e. when the interface shrinkage only increases

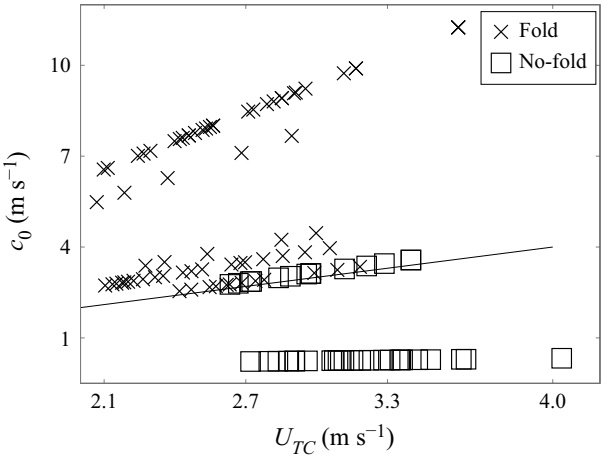

Figure 4. Key velocities: theoretically evaluated soap film retraction velocity U_{TC} versus elastic wave propagation velocity c_0. The solid line corresponds to $c_0 = U_{TC}$.

the surface surfactant concentration Γ without affecting the bulk concentration, is justified by the fact that the characteristic time of the interface shrinkage $t_{exp} = l/U_{TC} = O(10^{-2})$ s is much shorter than the characteristic times of desorption $t_d = k_d^{-1} \sim 0.2$ s and adsorption $t_a = \Gamma/(k_a C) \sim 0.2$ s. The values of the adsorption $k_a = 0.64 \times 10^{-5}$ m s^{-1} and desorption $k_d = 5.87$ s^{-1} coefficients are calculated via fitting (Fernandez *et al.* 2005) the Langmuir–Hinshelwood equation, $\mathrm{d}\Gamma/\mathrm{d}t = k_a C(1-\theta) - k_d\Gamma$, with $\theta = \Gamma/\Gamma_m$ being the fractional coverage and $\Gamma_m = 10^{-5}$ mol m^{-2}, to the experimental data (Chang & Franses 1992). When the surfactant concentration increases (thus lowering the surface tension) or glycerol concentration decreases (and thus the viscosity as well), the thickness of the soap film decreases and U_{TC} approaches c_0, with the resultant pattern transitioning from fold to no-fold. The solid line in figure 4 corresponding to $c_0 = U_{TC}$ convincingly marks this transition.

In support of the conclusions drawn from the map in figure 4 – namely, that folds are observed only for $c_0 > U_{TC}$ – two sets of direct measurements of the soap film retraction U_{TC} and SW propagation c_0 speeds were carried out: (i) when the concentration of SDS was fixed at 0.5 CMC with the concentration of glycerol varied between 5 and 25 % wt in figure 5(*a*); and (ii) when the concentration of glycerol was set at 20 % wt with the SDS concentration changed in the range 0.5–1.25 CMC in figure 5(*b*). In both cases, five withdrawal velocities were implemented in the course of the experiments. In figures 5(*a*) and 5(*b*) the measured U_{TC} and c_0 are shown with white and black symbols, respectively, confirming that the fold regime corresponds to the condition $c_0 > U_{TC}$. The theoretical estimates of the retraction terminal velocity U_{TC} are represented with grey symbols.

In both figures 5(*a*) and 5(*b*), there is some deviation between the theoretical and measured U_{TC}, which is due to a number of competing factors. First, the film thickens after the SW and hence U_{TC} decreases compared to that evaluated at the initial (equilibrium) film thickness h_∞ in front of the SW. Second, the surfactant monolayer is compressed between the SW and the retracting edge, thus decreasing the surface tension in this area, compared to the surface tension of the original soap film, and hence U_{TC}. Third, owing to the difference in surface tension before and after the SW, there is a Marangoni

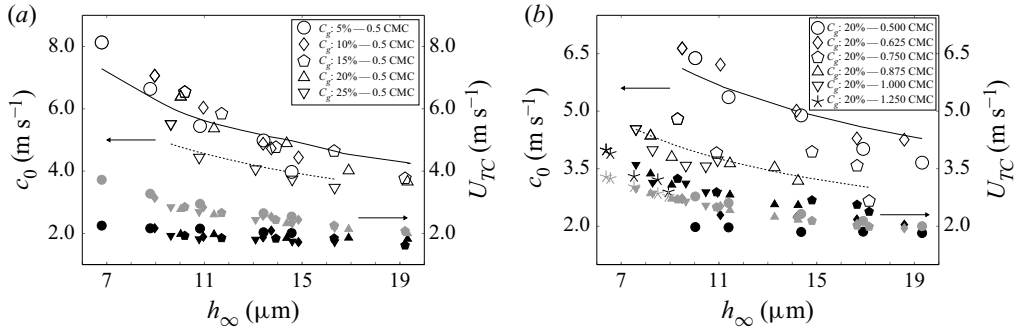

Figure 5. Key measured velocities for the case of fold formation. Panels (*a*) and (*b*) demonstrate c_0 and U_{TC} for different soap films. (*a*) The wave propagation c_0 and soap film retraction U_{TC} velocities for different soap films prepared at 0.5 CMC of SDS and five concentrations of glycerol (5, 10, 15, 20 and 25 % wt): for each of them, five different withdrawal velocities were applied, which resulted in 25 soap film thicknesses. To guide the eye, we added the solid curve $c_0 = \sqrt{2E/\rho h_\infty}$ fitted to 5, 10, 15 and 20 % wt glycerol data points, yielding $E = 0.182$ N m^{-1} and the dashed curve fitted to 25 % wt glycerol data points, producing $E = 0.121$ N m^{-1}. The white and black symbols represent the measured wave propagation and the soap film retraction velocities, respectively. The grey symbols correspond to the theoretically evaluated U_{TC}. (*b*) The wave propagation and soap film retraction velocities for different soap films with glycerol concentration fixed at 20 % wt. Surfactant concentration is changed in this set of experiments from 0.5 to 1.25 CMC. The solid line is a fitted curve c_0 to 0.5 and 0.625 CMC data points, yielding $E = 0.186$ N m^{-1}; and the dashed line is a fitted curve to 0.75, 0.875 and 1 CMC velocity data points, yielding $E = 0.082$ N m^{-1}. At 1.25 CMC the fold pattern was not observed, and hence data for c_0 for this concentration cannot be shown in panel (*b*).

force accelerating the soap film edge and thus increasing U_{TC}. Given this understanding, in figure 5(*a*) we can see that, due to the substantial difference between U_{TC} and c_0, the monolayer is not substantially compressed, so that the effect of film thickening after the SW overcomes that of the Marangoni force and hence the theoretical U_{TC} overpredicts the measured values. This trend can also be partially discerned in figure 5(*b*) for 0.5 CMC and some of the 0.625 CMC points, but for other SDS concentrations, due to weaker compression of the monolayer (as measured by smaller difference between U_{TC} and c_0), film thickening is overtaken by the initially subdominant Marangoni effect leading to higher measured values of U_{TC}.

Lastly, there is also a concomitant inhibiting effect due to friction between air and the retracting part (aureole) of the soap film as happens in all soap film flows (Couder *et al.* 1989). In our case, however, the dissipation due to the presence of the air phase is negligible, which can be seen from the corresponding ratio of damping forces due to the film (bulk μ_{film} and surface $\mu_{surface}$) viscosities and the air viscosity μ_{air}, i.e. $F_{film}/F_{air} \sim 2\rho_{air}\sqrt{\nu_{air}UL^3}/(\mu_{film}h_\infty + 2\mu_{surface}) = O(10)$ (cf. formula (39) in Couder *et al.* 1989), evaluated for typical values in our experiments, namely, $L = 5$ cm, $U = 5$ m s^{-1}, $\mu_{film} = 10^3$ Pa s and $h_\infty = 10^{-5}$ m. In this formula we took $\mu_{surface}$ to be the dilatational surface viscosity $\kappa = 10^{-5}$ N s m^{-1} (Wantke, Fruhner & Örtegren 2003), as most of the surface of the collapsing soap film is subject to dilatation only (Edwards, Brenner & Wasan 1991), rather than shear (which takes place only near the folds). In any case, dilatation viscosity has the dominant effect compared to that due to the shear $\mu_s \approx 5 \times 10^{-6}$ N s m^{-1} and bulk $\mu_{film}h_\infty \approx 10^{-8}$ N s m^{-1} viscosities. Therefore, for example, the lower measured values of U_{TC} compared to the theoretically predicted ones in figure 5(*a*) are not due to the retarding effect of the air, but primarily are due to

the film thickening after the SW compared to the initial (before the soap film release) film thickness.

3.2. *Mechanism*

The experiments reported above identify the necessary kinematic conditions for the occurrence of folds, but do not address the crux of the problem – the question of the origin of the dynamic folds. The subsonic nature of the folds, $U_{TC} < c_0$, delineates them from SWs in aerodynamics and hence the underlying mechanism must be different. This becomes obvious from yet another discovered key condition for the observed phenomena: the enigmatic effect of the soap film frame corner when experiments were conducted on frames with sharp (figure 6*a*) and smoothed out (figure 6*b*) corners under otherwise the same conditions. Evidently, the curvature of the frame corner directly affects the outcome soap film pattern: the fold pattern is observed for the sharp 90° corner, while in the case of the smoothed corner no fold pattern is formed in the course of the soap film retraction.

The appearance of folds, at least visually, might be thought of as related to some sort of buckling. The first candidate is the buckling instability of a sheared thin viscous film, cf. Benjamin & Mullin (1988) and Slim, Teichman & Mahadevan (2012), to name a few. If one considers a fluid element travelling from the soap film edge towards the diagonal (cf. figure 8*c*), it is clear that it will experience both rotation $\omega_z = (\partial v/\partial x - \partial u/\partial y)/2$ and shear (strain) $\varepsilon_{xz} = (\partial v/\partial x + \partial u/\partial y)/2$, though the shear is compensated by rotation as $\partial v/\partial x = 0$ (note that $\partial u/\partial y \neq 0$ because $u = 0$ before reaching the diagonal and $u = v$ upon reaching it due to symmetry); here u and v are the x and y components of the velocity vector. Despite the fact that shear of the base soap film flow is indeed present at the diagonal, it does not propagate into the interior of the soap film, as is seen from figure 8(*a*,*c*) and hence no buckling instability is observed. Moreover, as figure 6(*b*) demonstrates, when the corner is smoothed out, no folds are formed in spite of the fact that shear must still be present along the diagonal. Hence shear-induced buckling cannot be deemed responsible for fold formation.

Second, the observed wave propagation is closely related to the nature of the surfactant molecules, which have polar and non-polar ends and therefore form a monolayer at the interface between a polar substance such as water and a non-polar one such as air. The surfactant monolayer separates the two substances and reduces surface tension. As happens in our experiments on collapsing soap films, under compression, a surfactant monolayer may experience a mechanical instability, similar to the buckling instability of a beam or a plate, with the wavelength of the surface undulations in the range of 1–10 μm and amplitude of a few nanometres (Milner, Joanny & Pincus 1989; Saint-Jalmes & Gallet 1998), which makes them inadequate to explain the observed folds, as the latter apparently have a much larger amplitude. The velocity of the associated wave propagation in surfactant monolayers is dictated by their compressibility (Griesbauer, Wixforth & Schneider 2009) and could be of the order of 10^2 m s^{-1}. While we cannot observe nanometre-amplitude deformations on the soap film surface, the optical properties of the surfactant monolayer change drastically under compression, which may lead to the discernible dark region, i.e. 'aureole' (cf. figure 7). Because of the surfactant used in our experiments (SDS), its monolayer compressibility properties (Khattari *et al.* 2011) allow for significantly lower wave propagation speeds c_0, making them comparable to the edge retraction speeds U_{TC}, thus enabling the phenomena presented here: transition from no-fold to fold regime. We should also note that for the two concentrations of surfactant (0.875 and 1 CMC) an aureole is developed on the soap film surface (figure 7), while for

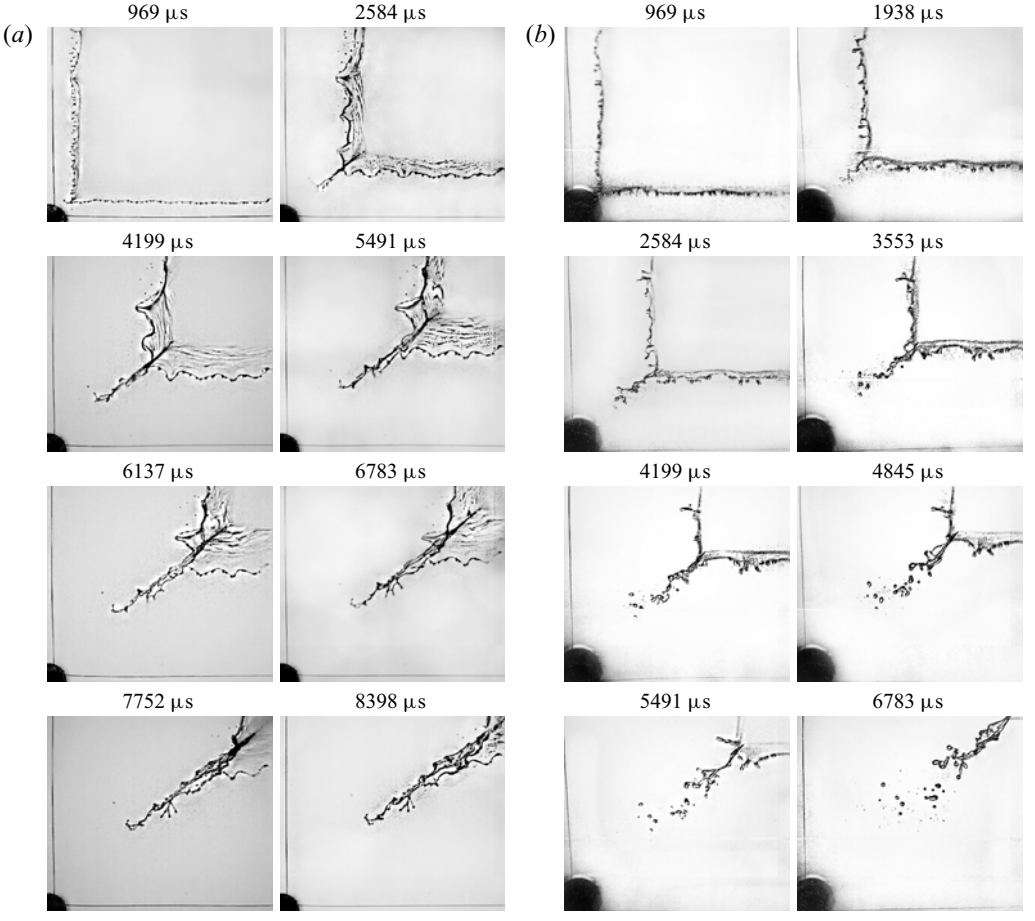

Figure 6. Time sequence of the soap film retraction demonstrating the effect of frame corner (a quarter of the soap film area is shown). In the time sequence shown in (*a*), the corners of the frame are sharp 90°, while in the set of images shown in (*b*) the 90° frame corners are smoothed out. Soap film solution properties: 1 CMC of SDS, 20 % wt glycerol; the soap film thickness and withdrawal velocity are 10.5 μm and 12.4 mm s^{-1}, respectively. The physical image size is 22 mm × 19 mm.

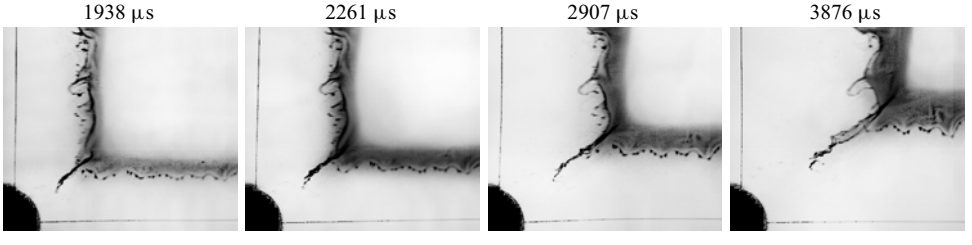

Figure 7. Time sequence of the soap film retraction to show the appearance of a dark region on its surface with the camera zoomed on a quarter of the film area. The dark region develops as the SW propagates on the soap film surface. Soap film solution properties: 0.875 CMC of SDS, 20 % wt glycerol. Withdrawal velocity and film thickness are 9.1 mm s^{-1} and 11.4 μm, respectively. The physical image size is 22 mm × 19 mm.

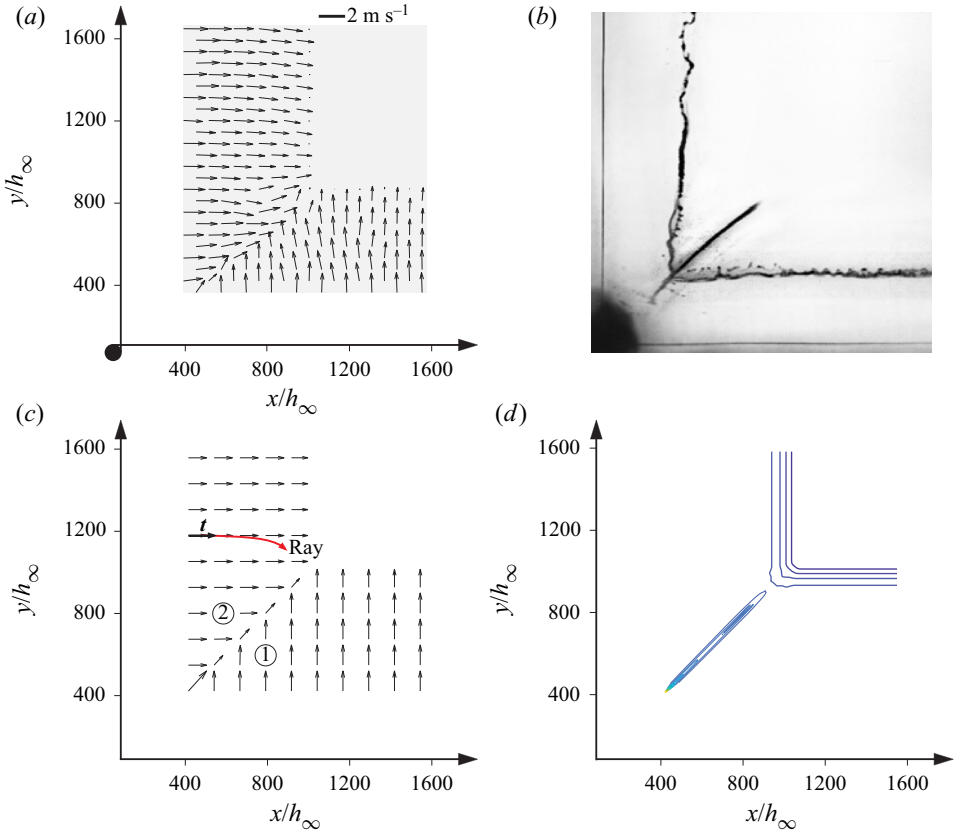

Figure 8. Experiments versus theory. (*a*) PIV velocity field acquired 2.4 ms after the triggering pulse. The time difference between the two PIV images is 100 μs. The size of the grey area is 19.8 mm × 22 mm. The experimentally measured one-dimensional shock and retraction velocities are $c_0 = 4.02\ \mathrm{m\ s^{-1}}$ and $U_{TC} = 1.86\ \mathrm{m\ s^{-1}}$, respectively. (*b*) Fold formation on the soap film 2.6 ms after the triggering pulse. The physical image size is 22 mm × 22 mm. The soap solution in (*a*,*b*) consists of ultrapure water, 20 % wt glycerol and 0.5 CMC of SDS. The soap film thickness and withdrawal velocity are 16.9 μm and $12.4\ \mathrm{mm\ s^{-1}}$, respectively. (*c*) Numerical result for the velocity field distribution on the soap film in the presence of fold. (*d*) Contour plot of numerically calculated $h(t, x, y)$ for the conditions corresponding to those in panel (*c*).

low concentrations (0.5 and 0.625 CMC) we have not observed any darkening (figure 2*a*), though a compressed surfactant monolayer may not always be visible. Yet, the higher SDS concentration 1.25 CMC implies no SW propagation and hence no aureole (figure 2*b*), while at low SDS concentrations there are not enough surfactant molecules at the interface to darken the film.

4. Theory

Given the inability of the known phenomena – buckling of sheared thin viscous films and compressed monolayers – to expound the origin of folds, we must turn to the fundamental description of the soap film dynamics in our setting. Since the subsonic soap film dynamics, $U_{TC} < c_0$, alone is not sufficient to explain the origin of folds, further insights are needed into the underlying mechanisms, which is done in this section with theoretical tools. First, we identify the soap film dynamical model, the numerical solution

of which (§ 4.1) replicates the experimental observations of the velocity field and soap film thickening along the diagonal. With confidence in the model thereby built, we are then able to extract the SW relations (§ 4.2) and the phenomena on the diagonal leading to folds (§ 4.3), also contributed by acoustic effects (§ 4.4).

4.1. *Soap film dynamics*

In the Cartesian (x, y) coordinates corresponding to the soap film plane, the continuity and momentum conservation equations governing the soap film dynamics (Wen & Lai 2003) with velocity $\boldsymbol{v} = (u, v)$ and thickness $h(t, x, y)$, written here in analogy to Euler's equations of ideal fluid motion (Landau & Lifshitz 1987), are

$$\frac{\partial h}{\partial t} + \boldsymbol{\nabla} \cdot (h\boldsymbol{v}) = 0, \tag{4.1a}$$

$$\frac{\partial (h\boldsymbol{v})}{\partial t} + \boldsymbol{\nabla}(h\boldsymbol{v} \otimes \boldsymbol{v} + h\hat{c}^2 \boldsymbol{I}) = 0, \tag{4.1b}$$

non-dimensionalized according to

$$h \to h_\infty h, \quad \boldsymbol{v} \to v_\infty \boldsymbol{v}, \quad x \to h_\infty x, \quad t \to (h_\infty / v_\infty) t, \tag{4.2}$$

where $\boldsymbol{I}$ is the unit tensor and $\hat{c} = c_0/v_\infty$ is the Marangoni elasticity speed scaled with respect to $v_\infty = U_{TC}(h_\infty)$. The existence of an elasticity-mediated speed of propagation, similar to that for sound speed, provides the means for generating SWs in soap films. The presence of the blob along the soap film edge is not crucial for our considerations – there are cases in soap film dynamics when a blob is not formed, for example in highly viscous films (Debrégeas, Martin & Brochard-Wyart 1995), in which an 'instantaneous' thickening of the film is observed due to elastic propagation. Thus the initial and boundary conditions at the soap film edge (rim) for (4.1) are posed, respectively, as

$$t = 0: \quad h(0, x, y) = 1; x_r = 0, u_r = 1; y_r = 0, v_r = 1; \tag{4.3a}$$

$$x = x_r(t): \quad u_r = \sqrt{h_\infty / h_r}; \quad y = y_r(t): \quad v_r = \sqrt{h_\infty / h_r}; \tag{4.3b}$$

above we have taken into account that the blob-free soap film rim moves with the speed $U_{TC}(h_r)$ corresponding to the film thickness h_r at the rim.

For numerical implementation, (4.1) can be rewritten as

$$W_t + G(W)_x + H(W)_y = 0, \tag{4.4}$$

where G and H are nonlinear functions of W:

$$W = \begin{bmatrix} h \\ hu \\ hv \end{bmatrix}, \quad G = \begin{bmatrix} hu \\ hu^2 + F \\ huv \end{bmatrix}, \quad H = \begin{bmatrix} hv \\ huv \\ hv^2 + F \end{bmatrix}. \tag{4.5a–c}$$

In order to numerically integrate this two-dimensional soap film model, it is discretized as appropriate for solving nonlinear systems of hyperbolic conservative equations (Toro 1999) using finite differences with a backward scheme. First we integrate (4.4) by sweeping

in the x direction,

$$W_{i,j}^{n+1/2} = W_{i,j}^{n} + \frac{\Delta t}{\Delta x}(G_{i-1,j}^{n} - G_{i,j}^{n}), \tag{4.6}$$

and then, as is common in splitting schemes (Toro 1999), sweeping in the y direction,

$$W_{i,j}^{n+1} = W_{i,j}^{n+1/2} + \frac{\Delta t}{\Delta y}(H_{i,j-1}^{n} - H_{i,j}^{n}); \tag{4.7}$$

here the index n stands for the time stamp and indices i and j for mesh numbers in the x and y directions, respectively. For the system of equations (4.4), the Courant condition

$$\frac{\Delta t \max u}{\Delta x} + \frac{\Delta t \max v}{\Delta y} < 1 \tag{4.8}$$

allows one to choose the time step Δt as well as the spatial steps Δx and Δy in the x and y directions, respectively. The results of the numerical simulation after performing 80 time steps are reported in figure 8(*c*,*d*).

Modelling based on numerical implementation of (4.1) and (4.3) shows that the computed velocity field distribution in figure 8(*c*) is in good agreement with the experimental PIV measurements in figure 8(*a*). In figure 8(*c*), $\hat{c} = 2.3$ was chosen to fit the kinematics in figure 8(*a*), which is close to the experimental value $\hat{c} = 2.16$. A contour plot of the numerical solution of (4.1) and (4.3) for the film thickness $h(t, x, y)$ demonstrates a fold on the diagonal of the soap film as a result of wave propagation ahead of the retracting edge (cf. figure 8*d*) in analogy to the experimental observations in figure 8(*b*).

4.2. *Shock wave speed*

For convenience, here we consider the dimensional version of (4.1) with c being the elastic wave speed. When integrated across the surface of discontinuity, the mass conservation equation (4.1*a*) yields $[hv]_1^2 = 0$ for the difference in mass flux on either side of the SW (cf. figure 9*a*), which in the frame of reference associated with the moving SW (cf. figure 9*b*) reads (Landau & Lifshitz 1987)

$$ch_\infty = h_-(c - v_-); \tag{4.9}$$

in this formula, on the left-hand side, c plays the role of the velocity of the soap film of thickness h_∞ incoming onto (in front of) the SW, while, on the right-hand side, $c - v_-$ is the soap film velocity behind the SW and the corresponding soap film thickness is h_-. Equation (4.9) signifies some important properties: one must have $c > v_-$ and $h_- \neq h_\infty$. To (4.9) we should add a momentum conservation condition following from the conservative form of the differential momentum conservation equation (4.1*b*), i.e. $[h(v^2 + c^2)]_1^2 = 0$ in the frame of reference moving with the SW, thus producing

$$h_\infty(c^2 + c_\infty) = h_-[(c - v_-)^2 + c_-^2], \tag{4.10}$$

where we took into account that in general the SW speed c is different from the sound speed c_∞ in front of the SW and from c_- behind it. By eliminating $c - v_-$ from (4.9) and

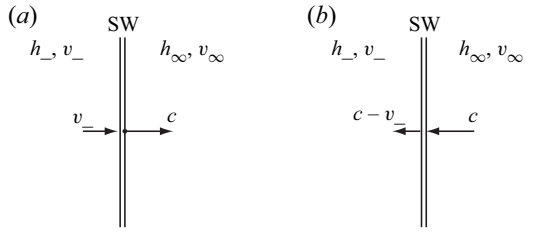

Figure 9. SW propagation in the laboratory (*a*) and moving (*b*) frames of reference.

(4.10), we find the (squared) SW speed

$$c^2 = \frac{h_-}{h_\infty}\,\frac{h_- c_-^2 - h_\infty c_\infty^2}{h_- - h_\infty}, \tag{4.11}$$

which tells us that, if the sound speed is calculated as for elastic waves, i.e. $c_\infty = \sqrt{E/\rho h_\infty}$ and similarly for c_-, then SW cannot form unless the elasticities E_∞ in front of and E_- behind the SW are different.

4.3. *Dynamics on the diagonal*

While the numerical solution in § 4.1 replicates the experimental observations, it does not provide deeper insights offered by an analytical study. To that end, using (4.1) we derive the Rankine–Hugoniot conditions analogous to SWs in aerodynamics (Landau & Lifshitz 1987) along the soap film diagonal Γ defined by $x = y$, where a fold is observed:

$$[hu]_1^2 \frac{\mathrm{d}y}{\mathrm{d}x} = [hv]_1^2, \tag{4.12a}$$

$$\left[h\boldsymbol{v}u + h\hat{c}^2 I_x\right]_1^2 \frac{\mathrm{d}y}{\mathrm{d}x} = [h\boldsymbol{v}v + h\hat{c}^2 I_y]_1^2; \tag{4.12b}$$

with the notation introduced 1 is the phase below and 2 above the diagonal (cf. figure 8*c*), $I_x = (1,\ 0)^{\mathrm{T}}$ and $I_y = (0,\ 1)^{\mathrm{T}}$. The analysis of (4.12) leads to

$$u_1 = v_1, \quad u_2 = v_2, \quad h_1 = h_2, \quad (\boldsymbol{\nabla} h)_1 = (\boldsymbol{\nabla} h)_2, \tag{4.13}$$

which are the natural conditions across the diagonal Γ due to the symmetry of the problem with respect to it. Effectively, the diagonal serves as an impermeable wall or, in fact, two impermeable walls in between which (on a set of measure zero) there exists a dynamics mostly independent of the rest of the soap film, because the initial perturbation of large enough amplitude at the corner is confined by the soap film flows on either side, and hence can evolve only along the diagonal without propagating sidewise. On the other hand, any perturbation coming from the edge of the soap film away from the corner decays quickly due to being non-confined. Since the diagonal has its own dynamics, it must be governed by the corresponding equations, which are naturally the same soap film equations (4.1), but collapsed on the diagonal. Since the system (4.1) is in a coordinate-free form, the equations on the diagonal straightforwardly follow from substitution of the gradient $\boldsymbol{\nabla}$ by the directional derivative ∂/∂_Γ along the diagonal Γ, analogous in spirit to Hadamard's method of descent (Hadamard 1923).

Moreover, the diagonal proves to be one of the characteristics. Indeed, the characteristic surface $\Omega(t, x, y)$ in the space of independent variables (t, x, y) is defined in the context of

proving the Cauchy–Kovalevskaya theorem: namely, an initial value (Cauchy) problem does not have a unique solution, and thus is ill-posed, if the initial data are given at $\Omega(t, x, y)$. This allows a straightforward determination of the characteristic surface by making a transformation from the original independent variables (t, x, y) to $\Omega(t, x, y)$, in which resolution of the governing partial differential equations (4.1) for the highest-order derivatives of the solution becomes impossible (Petrovsky 1954):

$$\begin{pmatrix} \Delta & h\Omega_x & h\Omega_y \\ c^2\Omega_x & h\Delta & 0 \\ c^2\Omega_y & 0 & h\Delta \end{pmatrix} \begin{pmatrix} h_\Omega \\ u_\Omega \\ v_\Omega \end{pmatrix} = 0, \tag{4.14}$$

where $\Delta = \Omega_t + u\Omega_x + v\Omega_y$. Hence, the characteristic determinant reads

$$h^2\Delta[\Delta^2 - c^2(\Omega_x^2 + \Omega_y^2)] = 0, \tag{4.15}$$

implying that the system (4.1) is hyperbolic with one of the characteristics being the instantaneous streamline $\Omega_t + u\Omega_x + v\Omega_y = 0$ – the diagonal Γ is one of them – while the other ones are dictated by the soap film 'compressibility' with some correction terms:

$$\Omega_t^2 + (u^2 - c^2)\Omega_x^2 + (v^2 - c^2)\Omega_y^2 + u\Omega_x(\Omega_t - \tfrac{1}{2}v\Omega_y) + v\Omega_y(\Omega_t - \tfrac{1}{2}u\Omega_x) = 0. \tag{4.16}$$

4.4. *Acoustic effects*

Further insights into the origin of folds can be gained with the help of geometric acoustics, the basic assumption of which (Landau & Lifshitz 1987) is that locally a sound wave $\phi(t, \boldsymbol{r}) = A(t, \boldsymbol{r})\,\mathrm{e}^{\mathrm{i}\psi(t,\boldsymbol{r})}$ with the wavevector $\boldsymbol{k} = \nabla\psi$ and frequency $\omega = -\partial\psi/\partial t$ can be considered plane (cf. figure 11*a*), provided the amplitude A and the wave direction $\boldsymbol{k}$ do not change appreciably over the sound wavelength $\lambda = 2\pi/|\boldsymbol{k}|$, i.e. $\lambda/L \ll 1$ relative to the characteristic length scale L of the phenomena at hand (the soap film span). Let us try to understand the fold formation in the soap film dynamics with the help of a single eikonal equation, which relates ω and $\boldsymbol{k}$ and is known to admit multivalued solutions corresponding to caustics. Taking into account the motion of the soap film itself (Kritikos 1967) with the velocity field $\boldsymbol{v} = (u, v)$ furnishes

$$\omega = c_0|\boldsymbol{k}| + \boldsymbol{v}\cdot\boldsymbol{k}, \tag{4.17}$$

which is a modification of the steady-state eikonal equation (Landau & Lifshitz 1987) $|\boldsymbol{k}|^2 = \omega^2/c_0^2$. While the general case $|\boldsymbol{v}| \sim c_0$ can be formally considered, in order to make the implications of the presence of the soap film flow transparent, let us treat the limit $|\boldsymbol{v}| \ll c_0$. Using the standard characteristic analysis for the first-order nonlinear partial differential equations (Zauderer 2006), we arrive at the acoustic ray equation:

$$\frac{1}{2}\frac{\mathrm{d}^2\boldsymbol{r}}{\mathrm{d}s^2} = \nabla(n^2) + \nabla n\,\boldsymbol{t}\cdot\boldsymbol{v} + n\,\boldsymbol{t}\cdot\nabla\boldsymbol{v} + \frac{\mathrm{d}}{\mathrm{d}s}(n\boldsymbol{v}); \tag{4.18}$$

above the velocity vector is scaled as $\boldsymbol{v} \to \boldsymbol{v}/c_0$, $\boldsymbol{t} = \mathrm{d}\boldsymbol{r}/\mathrm{d}s$ is the vector tangent to the ray, s the arclength, $n = \omega/c_0$ the refractive index and $\boldsymbol{t}\cdot\nabla\boldsymbol{v}$ the usual vector–tensor product:

$$\boldsymbol{t}\cdot\nabla\boldsymbol{v} = (x_s, y_s)\begin{pmatrix} u_x & u_y \\ v_x & v_y \end{pmatrix} = x_s(\boldsymbol{i}u_x + \boldsymbol{j}u_y) + y_s(\boldsymbol{i}v_x + \boldsymbol{j}v_y). \tag{4.19}$$

The first term on the right-hand side of (4.18) is responsible for the ray bending in the direction of decreasing sound speed c_0 or, equivalently, in the direction of increasing

refractive index n. Since $|\mathrm{d}^2\boldsymbol{r}/\mathrm{d}s^2| = \kappa(s)$ is the curvature of the ray, then, in the presence of an inhomogeneous refractive index $n = n(x, y)$, the ray bends in the direction of the gradient ∇n (e.g. for the ray in figure 8(*c*) the vector ∇n points towards the diagonal). On the soap film diagonal Γ, ∇n is discontinuous and thus the curvature $\kappa(s)$ is singular. While the first term on the right-hand side of (4.18) is of the potential field nature due to its gradient structure, the last three terms, when rewritten in the tensor notation and recalling that $\mathrm{d}/\mathrm{d}s = \boldsymbol{t}\cdot\nabla$, can be combined as

$$\nabla_j n t_i u^i + n t_i \nabla_j u^i + t^i \nabla_i (n u_j) = t^i [\nabla_j (n u_i) + \nabla_i (n u_j)], \tag{4.20}$$

where we have taken into account that the gradient ∇ is a covariant vector, while the velocity $\boldsymbol{v}$ is contravariant; lowering or raising the index is done with the help of a metric tensor $\boldsymbol{g}$, e.g. $g^{ij} t_i = t^j$. The expression in parentheses on the right-hand side of (4.20) can be recognized as the in-plane symmetric stress tensor $\tau_{ij} \equiv \nabla_j (n u_i) + \nabla_i (n u_j)$, though weighted with the refractive index n. Since the latter is positive, the dynamic effect of (4.20) on acoustic rays is mostly determined by the flow field $\boldsymbol{v}$ in the soap film, with the meaning of (4.20) being essentially the total force (in the soap film plane) acting on the oriented unit area with the normal $\boldsymbol{t}$. Because the velocity gradient $\nabla_j u_i$ in (4.20) is negligibly small away from the diagonal, the effect of the first term on the right-hand side of (4.18) is dominant.

In summary, all the considered acoustic effects – 'sound' speed c_0 decreasing towards the diagonal (since the film thickness h is larger there) as well as the soap film flow $\boldsymbol{v}$ – suggest that the acoustic rays will bend towards the diagonal of the soap film (§ 4.4).

5. Discussion

As the experimental observations indicate (§ 3) and, in agreement with the general theory of hyperbolic partial differential equations (Zauderer 2006), the singularity (discontinuity) at the sharp corner of the boundary propagates into the soap film interior along the diagonal, which is a characteristic (§ 4.3). This leads to the formation of a fold due to being confined by the soap film flow and by the convergence of acoustic rays (§ 4.4) emanating from the retracting soap film edges towards Γ; these converging to the diagonal acoustic waves prevent propagation of disturbances from the fold and hence its dissipation.

At the same time, in the case of smooth initial boundary conditions (figure 2*b*), i.e. when the corner is round, the characteristics – the instantaneous streamlines (§ 4.3) – still bunch up at the diagonal as the velocity field does (cf. figure 8*a*,*c*), but no visible discontinuity (fold) in the solution forms, at least initially (thus transpiring that acoustic effects are not the chief determining factor in the fold origin at short times). Nevertheless, the propagating acoustic fronts are capable of developing a SW-like structure even without the singularities in the initial data. Indeed, figure 10 demonstrates that the collapsing rectangular (not exactly square) soap film leads to the formation of a bridge (envelope-like pattern) at the moment when the acoustic wave fronts from the vertical (in the image) sides of the soap film experience a head-on collision. The nature of the bridge formation upon collision of acoustic fronts in figure 10 is easy to understand as, given enough time, the waves propagating with a lower 'sound' speed in the bridge area (due to increasing soap film thickness) are caught from behind by faster-travelling waves.

Having disentangled the intricate effects of different nature underlying the emergence of folds, we remark that the folds (figure 2*a*) are, in a sense, a subsonic phenomenon because the soap film edge velocity U_{TC}, and hence the velocities at all other points, are below the elastic wave speed c_0 as opposed to the supersonic SW phenomena previously

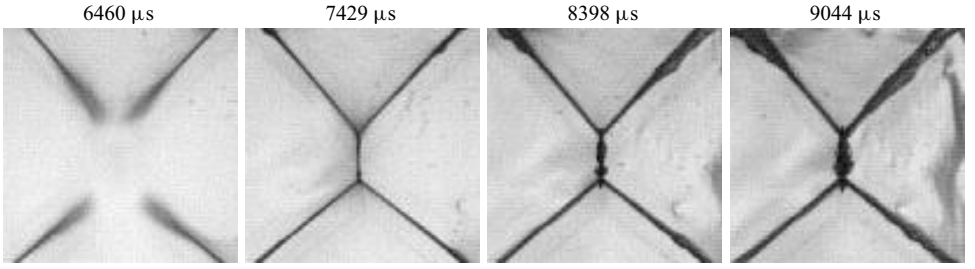

Figure 10. The bridge formation at the centre of a soap film. Soap film solution properties: 0.5 CMC of SDS, 5 % wt glycerol. The soap film thickness and withdrawal velocity are 14.6 μm and 16.1 mm s^{-1}, respectively. The physical image size is 11.7 mm × 11.7 mm.

observed/known to occur in soap films (Wen & Lai 2003; Wen *et al.* 2003; Tran *et al.* 2009; Kim & Mandre 2017). However, the magnitude of the velocity of retraction of the corner itself is $\sqrt{2}U_{TC}$ and may exceed c_0, so that the soap film velocity near the corner is supersonic. Indeed, while the solid line in figure 4 is shown for theoretically evaluated U_{TC} based on the measured film thickness h_∞, the actual measured $U_{TC}^{exp} = U_{TC}(h_-)$ is lower on average by 1.38 as per figure 5(*a*) (compare black versus grey symbols). Hence, the transition line corresponding to $c_0 = \sqrt{2}U_{TC}^{exp}$ in the coordinates of figure 4 would be $c_0 = 1.02U_{TC}$, i.e. very close to the solid line in the latter figure. Note that changes in the film thickness associated with the SW – it increases from h_∞ in front of SW to h_- behind it, which is substantial, as follows from the analysis of the soap film retraction speed in figure 5(*a*) – are not visible optically, meaning that the fold must be associated with a more significant film thickness variation. While away from the diagonal the SW propagates at speed c_0, the large-amplitude perturbation along the diagonal is capable of propagating at a higher speed $\sqrt{2}c_0$, for the SW speed depends on the SW amplitude (Landau & Lifshitz 1987).

In conclusion, we would like to point out that the physically realized folds and bridges on soap films in our experiments provide a lucid illustration of catastrophe theory (Arnold 2003). Thom's transversality theorem (Thom 1954, 1956), central in catastrophe theory (Arnold 2003) describing how continuous action produces a discontinuous result (Aubin 2004), tells us, in particular, about the forms the caustics may take. This theorem states (Wassermann 1974) that there exists only a finite number of types of structurally stable caustics – the 'elementary catastrophes' – for each value of the caustic codimension. The latter in our case is the dimension of the space onto which the two-dimensional acoustics on the soap film is mapped, which is one, as the fold type of singularities requires only a single coordinate to account for (cf. Appendix A).

Acknowledgements. The authors would like to thank H. Mayer for inspiring the present study and A. Stöckli at Astrol Electronic AG for providing a thyristor. R.K. is also grateful to A. Zelnikov for stimulating discussions.

Funding. This work was partially supported by the National Science Foundation (NSF) CAREER award under Grant No. 1054267, and by the Natural Sciences and Engineering Research Council of Canada (NSERC) under Grant No. 6186.

Declaration of interests. The authors report no conflict of interest.

Author ORCIDs.
Rouslan Krechetnikov https://orcid.org/0000-0001-6599-5000.

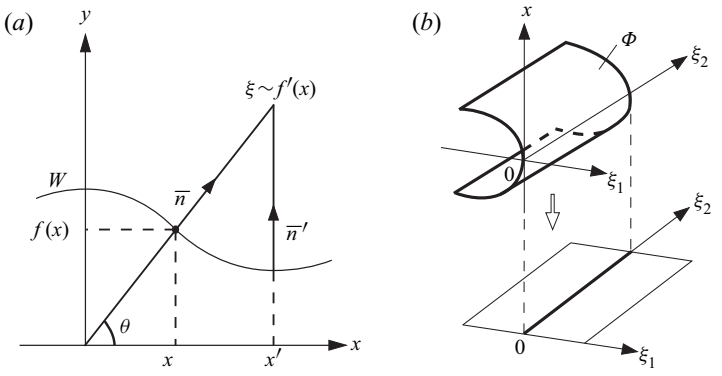

Figure 11. Geometric acoustics singularity. (*a*) Initial corrugated wavefront W and trajectories; and (*b*) fold formation, with $\xi_1 = \xi$ and ξ_2 being the dummy variable in our case.

Appendix A. Fold singularity

Following Berry (1976), let the wavefront at $y = 0$ be deformed into a surface W by lifting the part at x from $y = 0$ to $f(x)$ (cf. figure 11*a*), and assume that all radii of curvature of W are large in comparison with the wavelength λ to conform to the assumptions underlying geometric acoustics. We are interested in the far field of the waves originating from W, the directions of the trajectories of which contribute to the far field and can be specified by projections ξ on the x axis (figure 11*a*), i.e. by $\xi_x = \cos\theta$, where θ is the polar angle. The intensity $I(\xi)$ is defined by the flux through dξ far from W for a unit flux through unit area of W itself.

Each point x on W gives rise to a trajectory normal to W with the direction

$$\xi(x) = -f_x(x). \tag{A1}$$

For a given ξ there may be several points x satisfying this equation, which we label $x_i(\xi)$. Then the intensity is $I(\xi) = \sum_i |J(x_i, \xi)^{-1}|$ on the trajectory picture, where $J(x, \xi)$ is the Jacobian of the mapping (A1). The caustics of the family of trajectories travelling to infinity from W are the singularities of the mapping $x \to \xi$, i.e. they occur where $J(x, \xi)$ vanishes and I is infinite.

The application of Thom's theorem is made convenient by the fact that the trajectories (A1) can be derived from a generating function of the form $\Phi(x, \xi) = \xi x + f(x)$ by the gradient conditions $\Phi_x = 0$; then the caustics are singularities of these gradient maps. Thom's theorem concerns generic caustics, i.e. structurally stable in the dynamical systems sense (Wiggins 2003), meaning that a perturbation leaves the local structure of the caustic unchanged. The perturbed and unperturbed caustics are related by a diffeomorphism (a smooth reversible transformation). According to Thom's theorem (Wassermann 1974), there exist only a finite number of types of structurally stable caustics for each value of the dimensionality n of the control parameter space ξ, called the codimension of the caustic. Of immediate interest to us is only the first function generating a fold:

$$n = 1: \quad \Phi = x^3/3 + \xi x, \tag{A2}$$

illustrated in figure 11(*b*).

References

Adelizzi, E.A. & Troian, S.M. 2004 Interfacial slip in entrained soap films containing associating hydrosoluble polymer. *Langmuir* **20**, 7482–7492.

Almgren, F.J. Jr. & Taylor, J.E. 1976 The geometry of soap films and soap bubbles. *Sci. Am.* **231**, 82–93.

Arnold, V.I. 2003 *Catastrophe Theory*. Springer.

Aubin, D. 2004 Forms of explanation in the catastrophe theory of René Thom: topology, morphogenesis, and the structuralism. In *Growing Explanations: Historical Perspective in the Sciences of Complexity* (ed. M.N. Wise), pp. 95–130. Duke University Press.

Benjamin, T.B. & Mullin, T. 1988 Buckling instabilities in layers of viscous liquid subjected to shearing. *J. Fluid Mech.* **195**, 523–540.

Berg, S., Adelizzi, E.A. & Troian, S.M. 2005 Experimental study of entrainment and drainage flows in microscale soap films. *Langmuir* **21**, 3867–3876.

Berry, M.V. 1976 Waves and Thom's theorem. *Adv. Phys.* **25**, 1–26.

Birch, T. 1757 *History of the Royal Society*, vol. III. A. Millard.

Boys, C.V. 1890 *Soap Bubbles and the Forces Which Mould Them*. Society for Promoting Christian Knowledge.

Brenner, M.P. & Gueyffier, D. 1999 On the bursting of viscous sheets. *Phys. Fluids* **11**, 737–739.

Burkhardt, B. 2021 Soap-film and soap-bubble models. In *Physical Models: Their Historical and Current Use in Civil and Building Engineering Design* (ed. B. Addis), pp. 569–586. Ernst & Sohn Verlag GmbH & Co. KG.

Carnero Ruiz, C., Diaz-Lopez, L. & Aguiar, J. 2008 Micellization of Sodium Dodecyl Sulfate in glycerol aqueous mixtures. *J. Dispers. Sci. Technol.* **29**, 266–273.

Chang, C.-H. & Franses, E.I. 1992 Modified Langmuir–Hinshelwood kinetics for dynamic adsorption surfactants at the air/water interface. *Colloids Surf.* **69**, 189–201.

Couder, Y., Chomaz, J.-M. & Rabaud, M. 1989 On the hydrodynamics of soap films. *Physica* D **37**, 384–405.

Courant, R. & Robbins, H. 1941 *What is Mathematics?* Oxford University Press.

Culick, F.E.C. 1960 Comments on a ruptured soap film. *J. Appl. Phys.* **31**, 1128–1129.

Debrégeas, G., Martin, P. & Brochard-Wyart, F. 1995 Viscous bursting of suspended films. *Phys. Rev. Lett.* **75**, 3886–3889.

Douglas, J. 1931 Solution of the problem of Plateau. *Trans. Am. Math. Soc.* **33**, 263–321.

Dupré, M.A. 1867 Sixième memoire sur la theorie méchanique de la chaleur. *Ann. Chim. Phys.* **4**, 194–220.

Edwards, D.A., Brenner, H. & Wasan, D.T. 1991 *Interfacial Transport Processes and Rheology*. Butterworth-Heinemann.

Evers, L.J., Shulepov, S.Y. & Frens, G. 1996 Rupture of thin liquid films from Newtonian and viscoelastic liquids. *Faraday Discuss.* **104**, 335–344.

Faraday, M. 1851 Experimental researches in electricity. Twenty-fifth series. *Phil. Trans. R. Soc. Lond.* **141**, 7–28.

Fernandez, J., Krechetnikov, R. & Homsy, G.M. 2005 Experimental study of a surfactant-driven fingering phenomenon in a Hele-Shaw cell. *J. Fluid Mech.* **527**, 197–216.

Frankel, S. & Mysels, K.J. 1969 The bursting of soap films. II. A theoretical study. *J. Phys. Chem.* **73**, 3029–3038.

Gharib, M. & Derango, P. 1989 A liquid film (soap film) tunnel to study two-dimensional laminar and turbulent shear flows. *Physica* D **37**, 406–416.

Gibbs, J.W. 1928, 1931 *Collected Works*, vol. I. Longmans Green.

Griesbauer, J., Wixforth, A. & Schneider, M.F. 2009 Wave propagation in lipid monolayers. *Biophys. J.* **97**, 2710–2716.

Hadamard, J. 1923 *Lectures on Cauchy'S Problem in Linear Partial Differential Equations*. Dover Publications.

Huibers, P.D.T. & Shah, D.O. 1997 Multispectral determination of soap film thickness. *Langmuir* **13**, 5995–5998.

Incropera, F.P. & DeWitt, D.P. 2002 *Introduction to Heat Transfer*. John Wiley & Sons.

Isenberg, C. 1992 *The Science of Soap Films and Soap Bubbles*. Dover.

Johnston, B. 1935 Torsional rigidity of structural sections. *Civil Engng* **5**, 698–701.

Khan, H., Seddon, J.M., Law, R.V., Brooks, N.J., Robles, E., Cabral, J.T. & Ces, O. 2019 Effect of glycerol with sodium chloride on the Krafft point of sodium dodecyl sulfate using surface tension. *J. Colloid Interface Sci.* **538**, 75–82.

KHATTARI, Z., LANGER, U., ALIASKARISOHI, S., RAY, A. & FISCHER, T.M. 2011 Effects of soluble surfactants on the Langmuir monolayers compressibility: a comparative study using interfacial isotherms and fluorescence microscopy. *Mater. Sci. Engng* C **31**, 1711–1715.
KIM, I. & MANDRE, S. 2017 Marangoni elasticity of flowing soap films. *Phys. Rev. Fluids* **2**, 082001.
KRITIKOS, H.N. 1967 The eikonal equation in a moving medium. *Proc. IEEE* **55**, 442–443.
LANDAU, L.D. & LIFSHITZ, E.M. 1987 *Fluid Mechanics*. Pergamon.
LYKLEMA, J., SCHOLTEN, P.C. & MYSELS, K.J. 1965 Flow in thin liquid films. *J. Phys. Chem.* **69**, 116–123.
MAXWELL, J.C. 1878 Capillary action. In *Encyclopaedia Britannica*, 9th edition, vol. 5, pp. 56–71. A. & C. Black.
MAYER, H.C. & KRECHETNIKOV, R. 2010*a* The life of a free soap film. APS-DFD Poster no. 72.
MAYER, H.C. & KRECHETNIKOV, R. 2010*b* The life of a free soap film. APS-DFD Gallery of Fluid Motion no. 107.
MAYER, H.C. & KRECHETNIKOV, R. 2017 Liquid film dewetting induced by impulsive Joule heating. *Phys. Rev. Fluids* **2**, 094003.
MCENTEE, W.R. & MYSELS, K.J. 1969 The bursting of soap films. I. An experimental study. *J. Phys. Chem.* **73**, 3018–3028.
MILNER, S.T., JOANNY, J.-F. & PINCUS, P. 1989 Buckling of Langmuir monolayers. *Europhys. Lett.* **9**, 495–500.
MYSELS, K.J. 1964 Soap films and some problems in surface and colloid chemistry1. *J. Phys. Chem.* **68**, 3441–3448.
MYSELS, K.J. & COX, M.C. 1962 An experimental test of Frankel's law of film thickness. *J. Colloid Sci.* **17**, 136–145.
MYSELS, K.J., SHINODA, K. & FRANKEL, S. 1959 *Soap Films: Studies of their Thinning*. Pergamon.
NEWTON, I. 1704 *Opticks*. Smith and Walford.
PETROVSKY, I.G. 1954 *Partial Differential Equations*. Interscience Publishers.
PLATEAU, J. 1873 *Statique expérimentale et théorique des liquides soumis aux seules forces moléculaires*. Gauthier Villars.
PRANDTL, L. 1903 Zur Torsion von prismatischen Stäben. *Phys. Z.* **4**, 758–759.
RUSANOV, A.I. & KROTOV, V.V. 1979 Gibbs elasticity of liquid films, threads, and foams. *Progr. Surf. Membrane Sci.* **13**, 415–524.
SAINT-JALMES, A. & GALLET, F. 1998 Buckling in a solid Langmuir monolayer: light scattering measurements and elastic model. *Eur. Phys. J.* B **2**, 489–494.
SAVVA, N. & BUSH, J.W.M. 2009 Viscous sheet retraction. *J. Fluid Mech.* **626**, 211–240.
SLIM, A.C., TEICHMAN, J. & MAHADEVAN, L. 2012 Buckling of a thin-layer Couette flow. *J. Fluid Mech.* **694**, 5–28.
TAJIMA, K., MURAMATSU, M. & SASAKI, T. 1970 Radiometer studies on adsorption of surface active substance at aqueous surface. I. Accurate measurement of adsorption of tritiated Sodium Dodecylsulfate. *Bull. Chem. Soc. Japan* **43**, 1991–1998.
TAYLOR, G.I. 1959*a* The dynamics of thin sheets of fluid. II. Waves on fluid sheets. *Proc. R. Soc. Lond.* A **253**, 296–312.
TAYLOR, G.I. 1959*b* The dynamics of thin sheets of fluid. III. Disintegration of fluid sheets. *Proc. R. Soc. Lond.* A **253**, 313–321.
THOM, R. 1954 Quelques propriétés globales des variétés differentiables. *Commentarii Math. Helvetici* **28**, 17–86.
THOM, R. 1956 Un lemme sur les applications différentiables. *Bol. Soc. Mat. Mexicana* **2**, 59–71.
TORO, E.F. 1999 *Riemann Solvers and Numerical Methods for Fluid Dynamics*. Springer.
TRAN, T., CHAKRABORTY, P., GIOIA, G., STEERS, S. & GOLDBURG, W. 2009 Marangoni shocks in unobstructed soap-film flows. *Phys. Rev. Lett.* **103**, 104501.
WANTKE, K.-D., FRUHNER, H. & ÖRTEGREN, J. 2003 Surface dilatational properties of mixed Sodium Dodecyl Sulfate/Dodecanol solutions. *Colloids Surf.* A **221**, 185–195.
WASSERMANN, G. 1974 *Stability of unfoldings*, Springer Mathematical Notes, vol. 393. Springer.
WEN, C.Y., CHANG-JIAN, S.K. & CHUANG, M.C. 2003 Analogy between soap film on one-dimensional motion and gas dynamics. II. Experiments of shock waves in soap films. *Exp. Fluids* **34**, 130–180.
WEN, C.Y. & LAI, J.Y. 2003 Analogy between soap film and gas dynamics. I. Equations and shock jump conditions. *Exp. Fluids* **34**, 107–114.
WIGGINS, S. 2003 *Introduction to Applied Nonlinear Dynamical Systems and Chaos*. Springer.
ZAUDERER, E. 2006 *Partial Differential Equations of Applied Mathematics*. Wiley-Interscience.